Triple-lidar measurements of wind across a virtual rotor plane over a sea surface

Triple-lidar measurements of wind across a virtual rotor plane over a sea surface

M Nafisifard[1,*], J B Jakobsen[1], J T Snæbjörnsson[1,2], M Sjöholm[3] and J Mann[3]

[1]Dept. Mechanical and Structural Engineering and Material Science, University of Stavanger, Kjell Arholmsgate 41, Stavanger, Norway.
[2]Department of Engineering, Reykjavik University, Menntavegur 1 IS-101, Reykjavík, Iceland.
[3]Department of Wind and Energy Systems, Technical University of Denmark, Denmark.

E-mail: *mohammad.nafisifard@uis.no

Abstract. An improved understanding of the spatiotemporal characteristics of the wind velocity field above the sea surface will benefit the design of modern offshore wind turbines. This study examines wind velocity data recorded on a bow-tie-like measurement pattern, approximately covering a rotor area diameter of about 70 m. The measurement data are obtained by triple continuous-wave Doppler lidars (short-range WindScanners). Two of the instruments are installed on a stable platform in the form of a suspension bridge deck, whereas the third is stationed on the ground nearby. Data from sonic anemometers installed above the bridge deck are used to validate the wind characteristics observed by the lidars. The lidar measurement data are explored in terms of wind flow mapping, mean flow characteristics and co-coherences. The results demonstrate the difference between the co-coherence at lateral and vertical separations and also differences from the coherence model in the IEC standard. The results further show the potential of lidar measurements to provide new insight into mean wind flow and turbulence characteristics applicable for offshore wind turbine design.

1. Introduction

Knowledge of the spatiotemporal characteristics of the wind field above the sea surface is of key importance for the design of offshore wind turbines [1]. Remote wind sensing using wind lidars provides attractive possibilities to acquire this for the safe design of offshore wind turbines with respect to their response to wind loadings.

In the recent decade, remote wind sensing by lidars has found a wide range of applications in the wind energy industry, both using continuous-wave and pulsed lidars. For wind resource assessment and wind turbine wake studies, ground-based lidars are commonly adopted, as discussed in e.g. [2, 3]. Measurements in complex terrain are often supported by numerical flow modelling [4]. For optimized power production and wind turbine control, lidars are installed on a wind turbine nacelle, [5, 6]. Offshore lidar wind measurements have been carried out from fixed platforms [7] or bottom-fixed wind turbines [8], as well as from floating platforms, such as buoys or ships [9]. Both a single [10] and multiple [11] lidars have been adopted to access the lateral wind coherence offshore. However, most previous offshore studies have been focused on 2D measurements, usually ignoring the vertical component, which is considered in the present work.

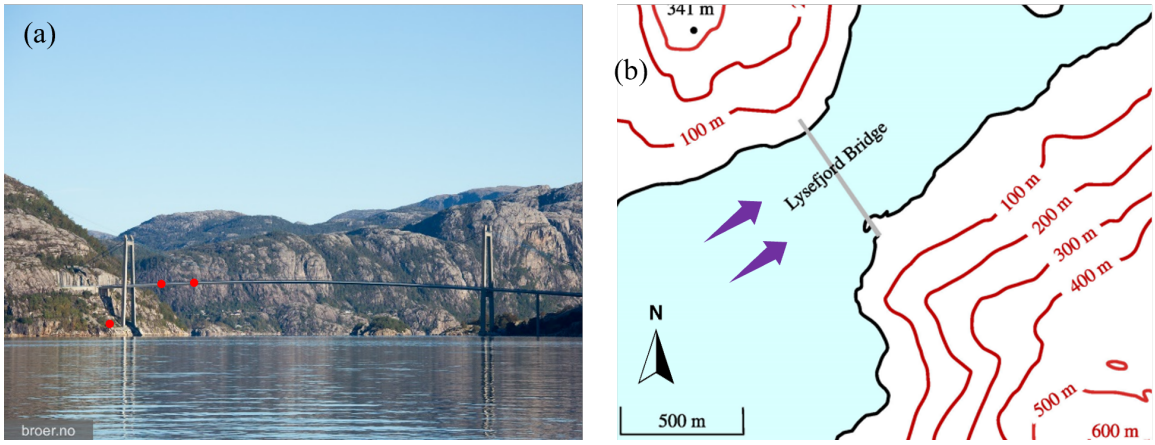

Figure 1. The Lysefjord Bridge. (a) View from the East, with lidar locations marked by red points. (b) Overview and position on a map, from [14].

The present work investigates the application of three synchronized continuous-wave lidars, for spatiotemporal mapping of turbulent flow above the sea surface. It has been developed within the Marine Renewable Infrastructure Network for Enhancing Technologies 2 (MARINET2), H2020 programme, as part of the project entitled Marine Atmospheric Coherence Assessed by Lidars – MACAL.

The objectives of the study are to verify the capability of lidar measurements to monitor the three wind velocity components, evaluate the wind field characteristics along an arbitrary radial direction in a "rotor plane", investigate the uniformity of the inflow as well as the first and second-order wind statistics including the turbulence spectra for all three turbulence components. In particular, the frequency-dependent correlation of wind fluctuations across a rotor plane (coherence) is estimated for vertical, radial, and lateral cross-wind separations. This remote sensing approach provides a unique advantage since the lateral coherence has not been properly observed from offshore measurement masts, where the anemometers are mainly aligned in the vertical direction.

The paper is organized as follows: Section 2 describes the measurement platform and the lidar measurement setup. Section 3 discusses the methods used to retrieve wind velocities from lidar recordings and the associated error propagation. Section 4 presents the mapping of the wind flow, a comparison of sonic and lidar observations, and the wind and turbulence characteristics. Finally, the main findings and conclusions of the measurement campaign are summarised in section 5.

2. Measurement Platform and the Monitoring System

In this study, a methodology for remote sensing of wind turbulence above the sea surface is tested by deploying a WindScanner measurement system from a transparent but stable platform, in the form of a suspension bridge deck (Figure 1a), 54 m above the sea surface, in a measurement domain spanned by a virtual wind turbine rotor. The platform is located in a fjord where the wind from the southwestern direction is favorable for inflow studies, as indicated by the arrows in Figure 1b. The flow was successfully monitored by lidars in an undisturbed region away from the bridge deck in a previous measurement campaign with a dual lidar system [12, 13].

The wind field is examined using three synchronized continuous-wave lidars. Two of the lidars are deployed on the bridge deck 36 m apart. The third lidar is installed 38 m below the bridge deck, next to the tower foundation at the North end of the bridge and is positioned 10.5 m from the vertical plane defined by the two lidars on the bridge girder (Figure 2 and Figure 3a-c). All

Table 1. Properties of the Doppler wind lidar short-range WindScanner system installation.

Properties	Values
Shortest range	approx. 10 m
Longest range	approx. 200 m
Probe volume (FWHM)	2 m to 6 m (for R2D1 and R2D2), 4 m to 18 m (for R2D3)
Lidars LOS detection range	-46.8 $\mathrm{m\,s^{-1}}$ to +46.8 $\mathrm{m\,s^{-1}}$

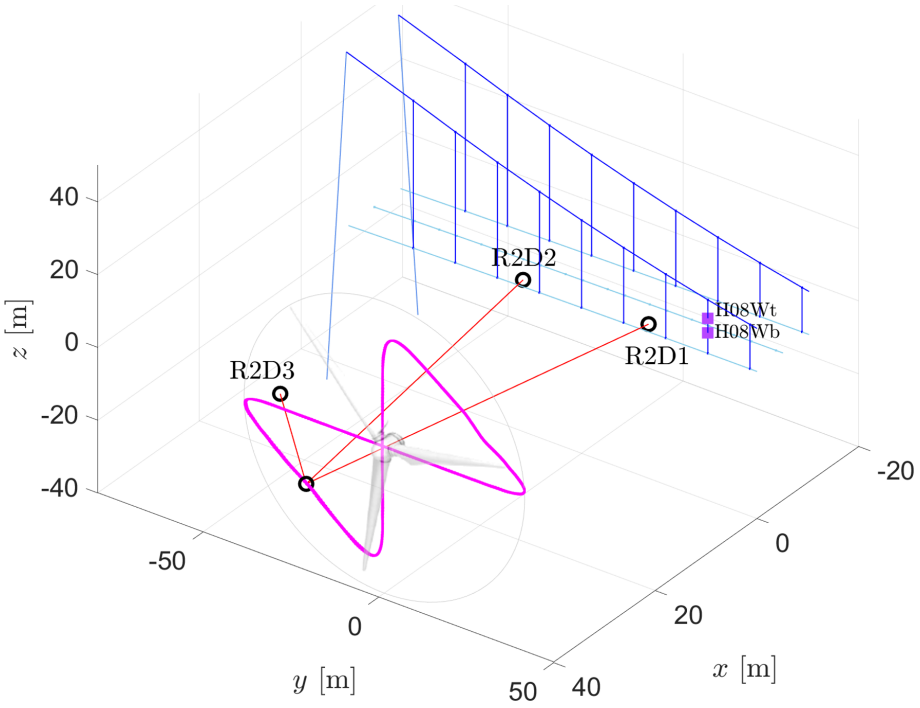

Figure 2. Lidar measurement setup.

three lidars have a 3-inch-wide optical telescope and a rotating double-prism head, allowing for scanning within a cone with a half-opening angle of about 61°. The WindScanner lidar system synchronizes the line-of-sight measurements made by the three lidar units, as they target a common dynamically steerable measurement "point", which makes it possible to retrieve all three velocity vector components of the inflow across a virtual rotor plane. The measurement domain is represented by a bow-tie-like scanning pattern in a vertical plane separated from the nose of the bridge deck by 40 m or ca. 3.25B, where B is the width of the bridge deck, which ensures flow measurements undisturbed by the bridge structure. The horizontal and vertical lines of the scanning pattern have a length of 80 m and 60 m, respectively. The measurement data along the bow-tie-like pattern are acquired with a sampling rate of 322.6 Hz and each scanning cycle takes one second, providing a temporal data resolution of about 1 second for each point on the pattern except for the point in the center of the bow-tie-like pattern which is revisited twice in a second, i.e., has a time-step of about 0.5 s. The key technical properties of the lidars are reported in Table 1. Also, more details about the instrumentation can be found in [15].

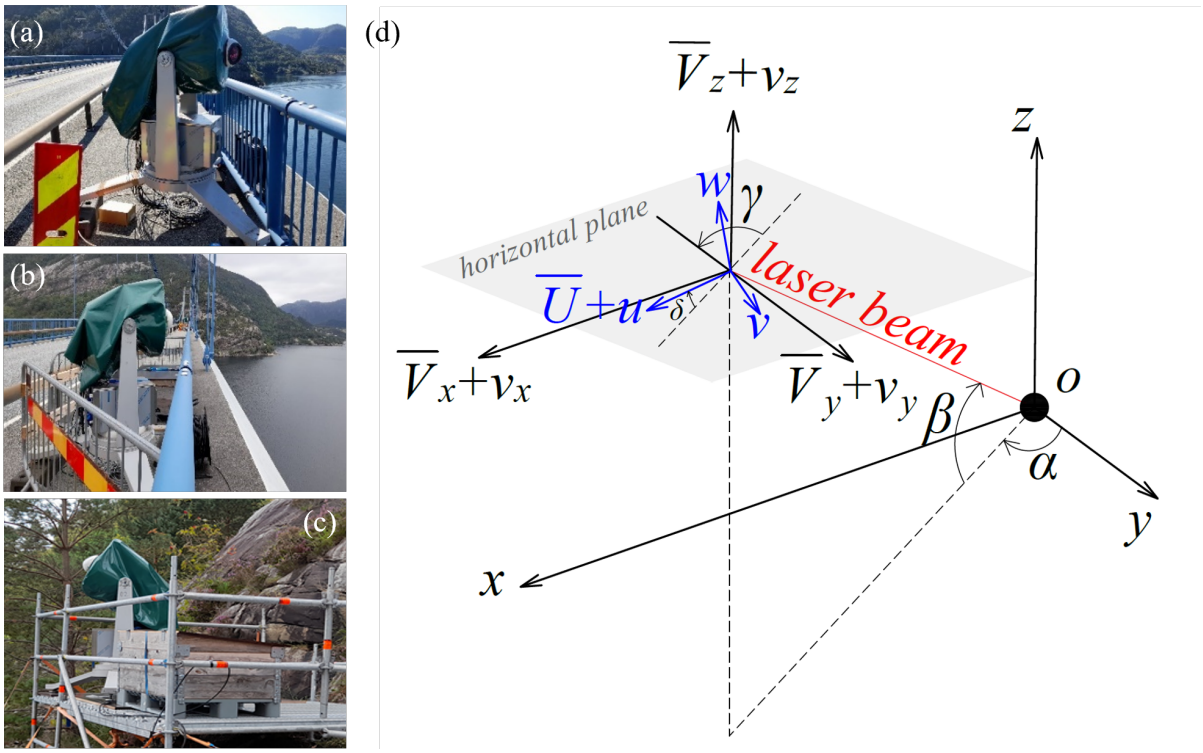

Figure 3. The triple-lidar system and the reference coordinate system. (a-c) Two deck lidars and one ground lidar. (d) Wind-based coordinate system.

3. Analysis Methods

3.1. Wind velocity formulation

With the three LOS velocities derived from Doppler spectra by the median frequency estimator, a geometric transformation can be applied to extract the 3D wind components:

$$\begin{bmatrix} v_x & v_y & v_z \end{bmatrix} = \begin{bmatrix} v_{LOS1} & v_{LOS2} & v_{LOS3} \end{bmatrix} \mathbf{M}^{-1} \tag{1}$$

In the above equation, the wind components normal and parallel to the deck are denoted by v_x and v_y, and the vertical component is denoted by v_z and $\mathbf{M}$ is defined as

$$\mathbf{M} = \begin{bmatrix} \sin(\alpha_1)\cos(\beta_1) & \sin(\alpha_2)\cos(\beta_2) & \sin(\alpha_3)\cos(\beta_3) \\ \cos(\alpha_1)\cos(\beta_1) & \cos(\alpha_2)\cos(\beta_2) & \cos(\alpha_3)\cos(\beta_3) \\ \sin(\beta_1) & \sin(\beta_2) & \sin(\beta_3) \end{bmatrix} \tag{2}$$

In equation 2, the azimuth and elevation angles are α and β, respectively. The angle between the main wind direction and the bridge axis, also called the yaw angle, is defined as:

$$\gamma = \arctan\left(\frac{\overline{v}_x}{\overline{v}_y}\right) \tag{3}$$

where $\overline{v}_x$ and $\overline{v}_y$ are the average of the across-deck and along-deck wind components. The wind-based coordinate system is illustrated in Figure 3d. Finally, the inclination angle, which is the angle of the wind direction and the horizontal plane, is defined by δ as:

$$\delta = \arctan\left(\frac{\overline{v}_z}{\sqrt{\overline{v}_y^2 + \overline{v}_x^2}}\right) \tag{4}$$

where, $\overline{v}_z$ is the average of the vertical wind component. The calculated wind components v_x, v_y, and v_z are rotated onto the main wind direction to obtain the along-wind ($\overline{U}+u$) as well as across-wind (v) and vertical wind (w) fluctuations where the mean values of u, v, and w are approximatively 0 $\mathrm{m\,s^{-1}}$. The vertical wind is thereby assumed as the summation of vertical mean wind velocity and zero-mean component i.e. $v_z = \overline{v}_z + w$ and along wind includes a vertical component.

3.2. The lidar data resolution

A Doppler wind lidar measures the radial velocity in a volume that is stretched along the beam and represented by the full width at half maximum (FWHM) [16]. The FWHM increases quadratically with the distance from the lidar to the observation point, as shown in equation (5).

$$\mathrm{Z_R} = \frac{\lambda r^2}{\pi a_0^2} \tag{5}$$

Here $\lambda = 1.565$ µm is the wavelength of the laser source; r is the measurement distance and $r_0 \approx 28$ mm is the beam radius. Accordingly, ground lidar (R2D3) measures the along-beam velocity within larger volumes due to its larger distance to the measurement domain; the FWHMs vary between 4.73 m and 17.25 m. The two deck lidars capture the LOS velocity with FWHMs, ranging between 2.36 m and 5.37 m.

3.3. Error propagation in the measurement

The accuracy of the results partly depends on the condition number of the matrix **M**, which reflects to what degree the vectors formed by the three lidar beams are linearly independent, i.e. to what degree the three light beams are not coplanar [17]. In this study, the condition number is at its largest value for the measurement location at the southern end of the horizontal line. However, in the whole domain it is below 10, which is a relatively small value and consequently, the wind velocity components can be reliably estimated using the designated measurement configuration.

4. Results

An 11-minute-long event, observed on 24$^{\mathrm{th}}$ September 2021, is chosen for the study presented in this paper. The wind direction was perpendicular to the measurement plane and there was no precipitation. For this wind event the sonic anemometer mounted 6 m above the bridge deck at hanger 8 (H08Wb), recorded a mean along-wind velocity of $\overline{U}$=5.91 $\mathrm{m\,s^{-1}}$, with the along-wind turbulence intensity of I_u=0.22 and vertical turbulence intensity of I_w=0.10. As the mean wind velocity is rather low, the turbulence intensity levels can be expected to be higher than is typical for offshore conditions [18, 19].

4.1. Wind flow based on WindScanner data

Figure 4 shows the fluctuating part of the incoming wind velocity and its variability along the horizontal line and vertical line of the scanning pattern. As can be seen, the velocity fluctuations along the two lines are consistent. The data illustrate the natural flow velocity variations, including occasional arrivals of large gusts, well correlated in the measurement domain. The along-wind turbulence intensity at the center of the bow-tie-like pattern is I_u=0.215. The associated mean wind speed is $\overline{U}$=6.0 $\mathrm{m\,s^{-1}}$, and the mean wind direction, with reference to bridge axis, is γ=267° for the point mentioned.

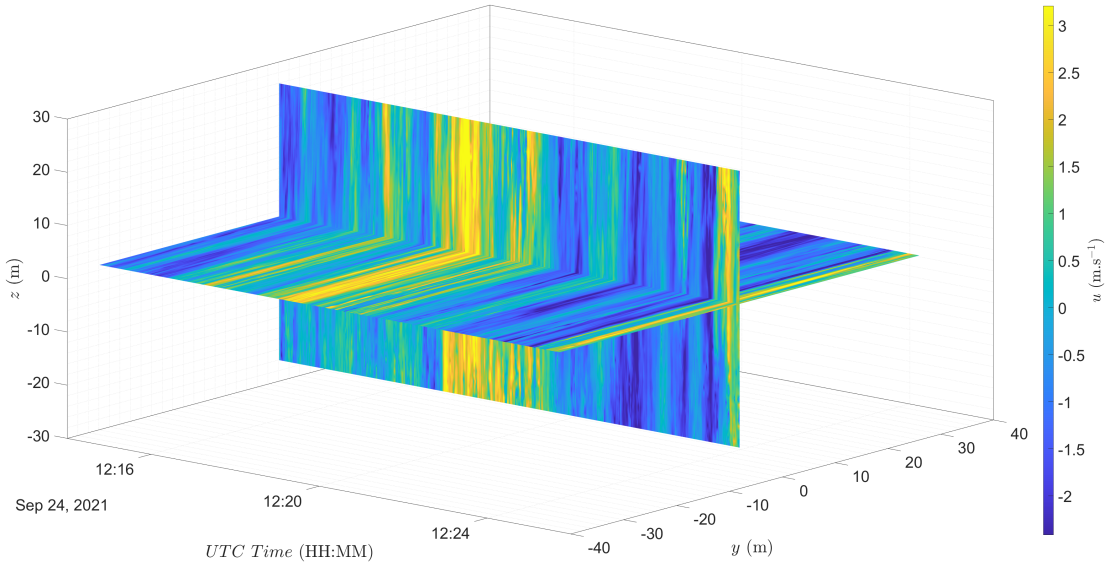

Figure 4. Mapping of the along-wind turbulence component, u, along the vertical and horizontal line of the scanning pattern.

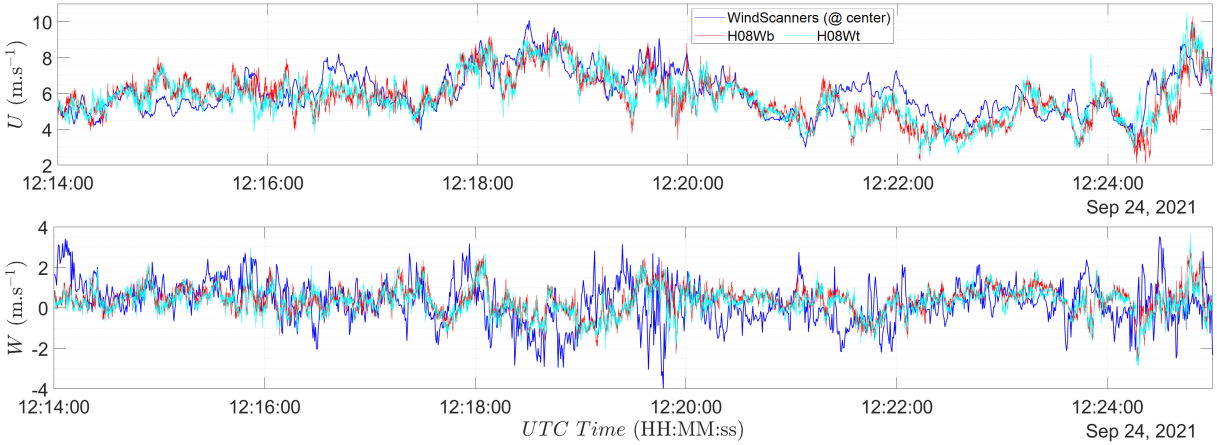

Figure 5. Along-wind and vertical wind components recorded by WindScanners at the center of the scanning pattern and anemometers located 40 m downwind.

4.2. Comparison of the sonic anemometer and lidar observations

The recorded lidar data at the center of the bow-tie-like pattern are compared to data from sonic anemometers installed 6 and 10 m above the bridge deck on hanger 8 (H08Wb and H08Wt), respectively. The sonic anemometers are located 36 m away from the pattern's center in deck-wise direction, close to the southern end of the horizontal scanning line, and 40 m downwind of the scanning line. Figure 5 displays the comparison of the along-wind and vertical components. A good agreement is seen between lidars and sonic data, except for somewhat larger variabilities in the vertical component obtained from lidar data, mainly because of measurement noise. A slight shift in phase is also observed in Figure 5, as a result of around 40 m distance between the scanning pattern and the sonic anemometers in the wind direction.

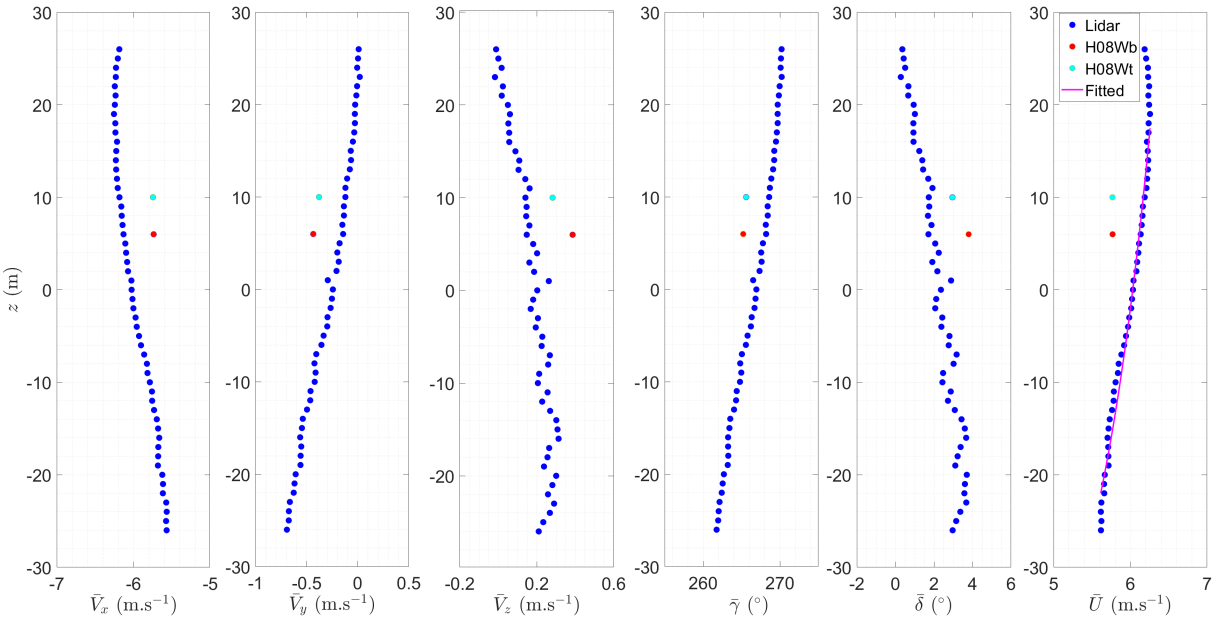

Figure 6. Profiles of across-plane, along-plane and vertical mean wind velocities, wind direction, inclination angle, and along-wind (from left to right), measured by the WindScanners along the vertical line of the scanning pattern compared to simultaneous measurements by anemometers. z=0 corresponds to 55.6 m above the sea surface.

4.3. Mean flow characteristics

The distribution of mean flow characteristics in space, along both the vertical and the horizontal line of the scanning pattern, is illustrated in Figure 6 and Figure 7, respectively. The mean wind speed in Figure 6 shows little variation at the top, and then it gradually reduces following the standard logarithmic profile. A logarithmic profile fitted to the values from ca. z=-26 m to z=+18 m is associated with roughness length and surface roughness coefficient of z_0=0.034 m and κ=0.003, respectively, which represents an open flat terrain category, rather than a sea surface [20]. This is likely because the wind passes over land before coming over the sea towards the lidars from the southwest. Also, a slight change in wind direction with height is observed with a direction becoming perpendicular to the measurement plane at the top of the scanning pattern. In Figure 7, a slight increase in the mean vertical wind speed towards the center of the fjord (positive y values), combined with a slight decrease in the mean wind speed, is associated with a modest increase in the inclination angle along the line, up to 4°.

4.4. Co-coherence

The spatiotemporal characteristics of natural turbulence above the sea surface are further studied in terms of the frequency-dependent correlation of wind velocity fluctuations across the measurement domain. The so-called co-coherence, which captures the in-phase variation of the velocity components at different frequencies, is estimated using the real part of the normalised cross-spectral density of wind components S_{ij}, simultaneously measured in two points, i and j:

$$CoCoh(f,d) = \frac{\mathrm{Re}(S_{ij}(f))}{\sqrt{S_i(f)S_j(f)}} \tag{6}$$

Here S_i and S_j are the auto-spectral densities of wind components in points i and j with a spatial separation $d = l_i - l_j$. In this study, the co-coherence of the along-wind component is

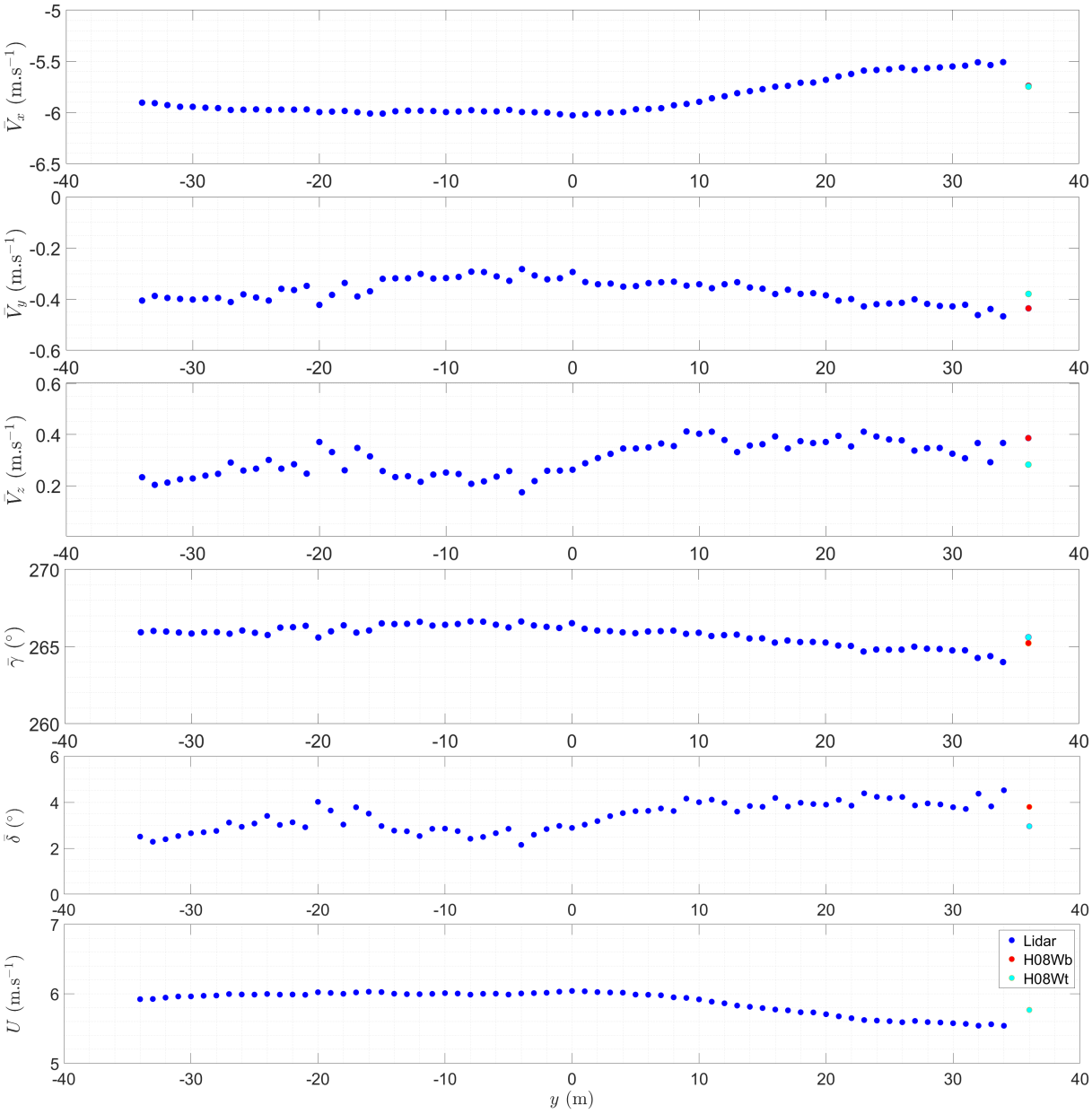

Figure 7. WindScanner observations along the horizontal scanning line and the corresponding anemometer data. The mean wind components shown and the location of origo (y=0 at hanger 5) is defined in Figure 3.

estimated using the Welch method by 50% overlapping [21] of five-minute segments. To acquire synchronized time series, the measurement domain is discretized into grid cells (also called clusters) of 1-meter length in z and y directions and then a linear interpolation in time is applied to the time-series for each spatial cluster containing data samples. The sampling frequency of interpolation is set to be 1 Hz for all data clusters which is close to the actual sampling frequency of the data within all clusters except at the center, where the sampling frequency is close to 2 Hz. This leads to a frequency range of 3 mHz to 0.5 Hz for the spectral density.

The resulting co-coherence estimates are displayed in Figure 8, for a selected separation of 10 m. The co-coherence is slightly weaker along the vertical line, compared to the horizontal

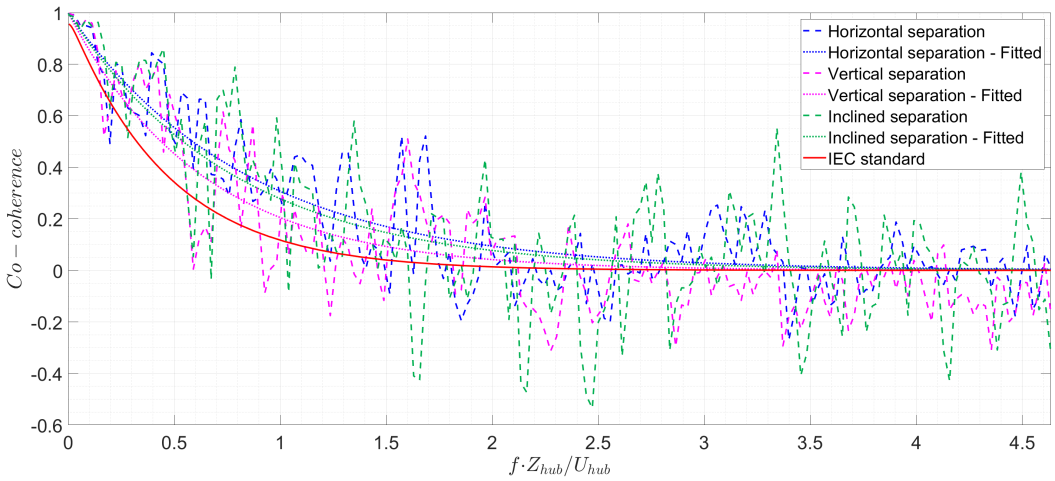

Figure 8. Co-Coherence measured (dashed line) by lidars, fitted (dotted line), and provided by standard (solid line) for separation of 10 m. z_{hub} and U_{hub} are equal to 56 m and 6.0 m s^{-1}.

line. As expected, the flow synchronisation for an arbitrary, "inclined" radial orientation, falls between that for the vertical and the horizontal direction. The samples used to establish the co-coherence for the inclined separation were defined in such a way that one end of the separation is positioned on the vertical line while the other end is on the horizontal line. This led to two inclined separations of 10 m for each quarter of the circular domain being observed, and eight samples for the entire domain in total, corresponding to ca. $\pm 53°$ or $\pm 37°$ with respect to the horizontal plane. The estimated co-coherence for horizontal separations indicates a positive smooth underlying function, expected for a limited separation of 10 m in a cross-flow. The vertical and the inclined coherence display some minor negative values, likely related to the wind shear.

For the studied separation, all three co-coherences are, in the following, compared to the exponentially decaying coherence function provided in the IEC standard [18]:

$$Coh(r,f) = \exp\left(-C_1\sqrt{\left(\frac{fr}{U_{\text{hub}}}\right)^2 + \left(\frac{C_2 r}{L_u}\right)^2}\right) \tag{7}$$

where U_{hub} is the wind speed at a hub height equal to 6.0 m s^{-1} and r is the across-flow separation. In the present study, the hub height (z_{hub}) is 56 m. The velocity component integral scale parameter, L_u, is taken as the integral length scale of the along-wind at hub height, which is found to be 202 m, for the data series used. C_1 and C_2 are here fitted to the estimated coherence data while the corresponding values given by IEC standard are included in the (last row of) Table 2.

The C_1 values are smaller than the value $C_1 = 12$ provided in the standard, indicating a higher level of turbulence synchronisation at the measurement site, which could excite a higher surge response of a floater compared to that associated with the standard coherence. The coherence for the vertical separations is slightly weaker than the one for the horizontal separations. As expected, the C_1 and C_2 values for inclined separations lie between the values for the vertical and horizontal separations. The estimated C2 coefficient, which defines the coherence at f $\simeq$ 0, is considerably lower than the value in the IEC standard. It is associated with a high level of uncertainty, following a limited duration of the studied event. It should be noted that the lidar measures the radial velocity in a volume that is stretched along the lidar beams. This volume sampling of the velocity may in principle result in a higher correlation between individual

Table 2. Estimated coefficients of the two-parameter exponential decay function.

	Separation = 10 m			**Separation = 20 m**		
		Coefficients			Coefficients	
	Samples	C_1	C_2	Samples	C_1	C_2
Vertical separations	43	8.9	0.002	33	9.2	0.002
Horizontal separations	59	6.6	0.008	49	6.4	0.011
Inclined separations	8	7.2	0.005	8	7.7	0.002
IEC standard	-	12.0	0.12	-	12.0	0.12

data points, especially in the present case where the separation is of a similar size as the lidar measurement volumes. In [13], consistent coherence estimates for lateral wind coherence were obtained using the sonic anemometers on the bridge and a dual lidar system. The present results, based on the triple lidar measurements, need to be further scrutinized, especially by studying the data for larger separations than the two reported in Table 2.

5. Conclusions

In this study, all three wind components of the wind field in a virtual wind turbine rotor area above the sea surface are examined using three synchronized continuous-wave lidars on a unique observation platform. The measurement domain was represented by a bow-tie-like scanning pattern in a vertical plane approximately 40 m upstream of the lidars. Each scanning cycle takes one second, providing a temporal data resolution of about one second for each spatial cluster on the scanning pattern. The main findings of this study are as follows:

- Lidar wind data in the tailored measurement setup capture well the wind field across the virtual rotor plane and the associated wind gustiness.
- Overall good agreement is seen between lidars and sonic measurements for along-wind and vertical velocity components except for somewhat larger variability in the vertical component obtained from the lidar data.
- The flow measurements were performed above the sea surface, with a few kilometres long fetch of water upstream of the monitored domain. Due to the complexity of the surrounding terrain, the recorded flow characteristics differ from those at an offshore site. The mean velocity profile shows a gradual increase with height, roughly following a standard logarithmic profile for open terrain, in agreement with the observed turbulence intensities.
- The coherence function of the same form as provided in the IEC standard was fitted to the lidar co-coherence estimates, for a separation of 10 m and 20 m along different "radial" directions. In the case studied, the co-coherence is found to depend on the orientation of the line of separation and is somewhat stronger than the one provided in the standard. For the horizontal lateral separation, the key decay coefficient of 8.9 was estimated, compared to 12.0 in the standard. Further data analysis is in progress, considering an extended data set and larger across-wind separations.

Acknowledgments

The authors acknowledge the support of the European Union Horizon 2020 through the Innovation Training Network Marie Skłodowska-Curie Actions: Lidar Knowledge Europe (LIKE (grant no. 858358)) and Marine Renewable Infrastructure Network for Enhancing Technologies 2, H2020, (MARINET2 (Grant no. 31084). We would also like to acknowledge the contributions of Michael

Courtney, Per Hansen, Claus Brian Munk Pedersen (Technical University of Denmark), Swen Roemer, Jarle Berge, Emil M. Surnevik, Caroline Einvik (University of Stavanger), and the Norwegian Public Road Administration (NPRA) in planning and conducting the measurement campaign. The authors are also grateful to Dr Etienne Cheynet from the University of Bergen for his valuable comments on the manuscript.

References

[1] Nybø A, Nielsen F G, Reuder J, Churchfield M J and Godvik M 2020 *Wind energy* **23** 1810–30
[2] Newmann J F, Bonin T A, Klein P M, Wharton S and Newsom R K 2016 *Wind energy* **19** 2239–54
[3] Kumer V, Reuder J, Svardal B, Sætre C and Eecen P 2015 *Energy Procedia* **80** 245–54
[4] Menke R, Vasiljevic N, Wagner J, Oncley S P and Mann J 2020 *Wind Energy Sci.* **5** 1059–73
[5] Fu W, Peña A and Mann J 2022 *Wind Energy Sci.* **7** 831–48
[6] Simley E, Fürst H, Haizmann F and Schlipf D 2017 *Remote Sen.* **10**
[7] Cañadillas B, Beckenbauer M, Trujillo J J, Dörenkämper M, Foreman R, Neumann T and Lampert A 2022 *Wind Energy Sci.* **7** 1241–62
[8] Cañadillas B, , Bégué A and Neumann T 2015
[9] Rubio H, Kühn M and Gottschall J 2022 *Wind Energy Sci.* **7** 2433–55
[10] Cheynet E, Jakobsen J B, Svardal B, Reuder J and Kumer V 2016 *Energy Procedia* **94** 462–77
[11] Cheynet E, Flügge M, Reuder J, Jakobsen J B, Heggelund Y, Svardal B, Saavedra Garfias P, Obhrai C, Daniotti N, Berge J, Duscha C, Wildmann N, Onarheim I H and Godvik M 2021 *Atmos. Meas. Tech.* **14** 6137–57
[12] Nafisifard M, Jakobsen J B, Cheynet E, Snæbjörnsson J, Sjöholm M and Mikkelsen T 2021 *IOP Conf. Ser.: Mater. Sci. Eng.* vol 1201 (IOP Publishing) p 012008
[13] Cheynet E, Jakobsen J B, Snæbjörnsson J, Mikkelsen T, Sjöholm M, Mann J, Hansen P, Angelou N and Svardal B 2016 *Exp. Fluids* **57** 1–17
[14] Cheynet E, Jakobsen J B, Snæbjörnsson J, Angelou N, Mikkelsen T, Sjöholm M and Svardal B 2017 *J. Wind Eng. Ind. Aerodyn.* **171** 261–72
[15] Nafisifard M, Jakobsen J B, Snæbjörnsson J, Sjöholm M and Mann J *J. Wind Eng. Ind. Aerodyn.* (Accepted for publication)
[16] Mikkelsen T 2009 *European Wind Energy Conference and Exhibition* vol 6 pp 4123–32
[17] Fuertes F C, Iungo G V and Porté-Agel F 2014 *J. Atmos. Oceanic Technol.* **31** 1549–56
[18] IEC61400-1 2005 *IEC 61400-1 Wind turbines, Part 1: Design requirements* (Norwegian electrotechnical publication)
[19] Türk M and Emeis S 2010 *J. Wind Eng. Ind. Aerodyn.* **98** 466–71
[20] Holmes J D 2015 *Wind loading of structures* vol 3rd edition (CRC Press)
[21] Welch P 1967 *IEEE Trans. Audio Electroacoust.* **15** 70–3